

Competing effects of wind and buoyancy forcing on ocean oxygen trends in recent decades

Received: 13 March 2024

Accepted: 16 October 2024

Published online: 26 October 2024

 Check for updates

Helene A. L. Hollitzer ^{1,2,3} ✉, Lavinia Patara ¹, Jens Terhaar ^{2,3} & Andreas Oschlies ^{1,4}

Ocean deoxygenation is becoming a major stressor for marine ecosystems due to anthropogenic climate change. Two major pathways through which climate change affects ocean oxygen are changes in wind fields and changes in air-sea heat and freshwater fluxes. Here, we use a global ocean biogeochemistry model run under historical atmospheric forcing to show that wind stress is the dominant driver of year-to-year oxygen variability in most ocean regions. Only in areas of water mass formation do air-sea heat and freshwater fluxes dominate year-to-year oxygen dynamics. The deoxygenation since the late 1960s has been driven mainly by changes in air-sea heat and freshwater fluxes. Part of this deoxygenation has been mitigated by wind-driven increases in ventilation and interior oxygen supply, mainly in the Southern Ocean. The predicted slowdown in wind stress intensification, combined with continued ocean warming, may therefore greatly accelerate ocean deoxygenation in the coming decades. The fact that the model used here, along with many state-of-the-art forced ocean models, underestimates recent ocean deoxygenation indicates the need to use forcing fields that better represent pre-industrial conditions during their spin-up.

Oxygen (O₂) is critical for sustaining marine life and regulates important elemental cycles in the ocean, such as those of nitrogen, phosphorus, and iron¹. Observations indicate that the global ocean dissolved O₂ inventory, currently estimated at 227.4 ± 1.1 Pmol², has decreased by >1%³ and possibly >2%² between 1960 and 2010, mainly in response to anthropogenic climate change. This deoxygenation is projected to continue in the coming decades, even under the low-emission, high-mitigation Shared Socioeconomic Pathways 1–2.6^{4,5} (SSP1–2.6) or a complete cessation of carbon dioxide emissions⁶. However, while there is a clear downward trend in the global oceanic O₂ inventory, regional O₂ responses to climate change vary widely across ocean basins and depths, implying spatial and temporal variability in the underlying drivers^{2,7}.

Ocean oxygen distribution and changes are the result of a complex interplay of driving forces that either enhance or deplete O₂. At the sea surface, ocean O₂ is in direct contact with the atmosphere through air-sea gas exchange. Thus, waters within the mixed layer are, to first order, in equilibrium with the O₂ partial pressure of the atmosphere, with the equilibrium oxygen concentration depending on the solubility of O₂ in seawater and, therefore, primarily on the sea surface temperature (SST). Beneath the mixed layer, there are no significant sources of oxygen, and O₂ can only be supplied by ventilation, defined as the physical processes by which (O₂-rich) surface waters are transferred from the surface mixed layer into the ocean interior. In the interior ocean, these water masses remain isolated from the atmosphere over long timescales set by the

¹GEOMAR Helmholtz Centre for Ocean Research Kiel, 24148 Kiel, Germany. ²Climate and Environmental Physics, Physics Institute, University of Bern, 3012 Bern, Switzerland. ³Oeschger Centre for Climate Change Research, University of Bern, 3012 Bern, Switzerland. ⁴Kiel University, 24118 Kiel, Germany.

✉ e-mail: helene.hollitzer@unibe.ch

interior transport patterns⁸, and their O₂ content is consumed by the respiration of organic matter.

The supply of oxygen to the ocean interior is not homogeneous across the global ocean, but is largely concentrated in specific locations of water mass formation^{8,9}. Ventilation is the result of a suite of interacting processes¹⁰, with the main atmospheric drivers being wind stress (i.e., the shear stress exerted on the ocean surface by wind) and air-sea heat and freshwater fluxes. Wind stress is a major driver of large-scale ocean circulation, and its divergence and convergence patterns force the gyre transports and the meridional overturning circulation^{11,12}. Air-sea heat and freshwater fluxes regulate the transformation of surface water masses and deep ocean mixing¹³. Prominent regions of ocean interior oxygenation include the subpolar North Atlantic, where strong surface buoyancy loss triggers open-ocean convection¹⁴, the coastal regions around Antarctica, where Antarctic Bottom Water is formed^{15,16}, and the regions of mode and intermediate water formation at mid-latitudes^{17,18}, especially in the Southern Ocean. These intensely ventilated regions can all be traced as oxygen maxima throughout the ocean interior¹⁹. As opposed to these well-ventilated oxygen maximum zones, poorly ventilated sites often result in oxygen minimum zones (OMZs), mostly located in the eastern part of the tropical oceans^{20,21}.

Anthropogenic climate change, manifested amongst other things by ocean warming²² and changing wind fields^{23,24}, has had far-reaching effects on ocean oxygen concentrations in recent decades. Ocean warming directly reduces oxygen solubility and accounts for about 15% of the global oxygen loss^{2,25}. Apart from the direct effect on solubility, anthropogenic warming also intensifies near-surface stratification²⁶, which is suggested to reduce ocean oxygenation by impeding the transport of O₂-rich surface waters into the permanent thermocline and by limiting the resurfacing of O₂-poor deeper waters, thereby reducing the intensity of O₂ uptake at the atmosphere-ocean interface²⁷. On the other hand, stronger stratification may also mitigate deoxygenation by reducing the upward transport of nutrients, thereby limiting biological production in the euphotic zone and the subsequent export and oxygen-consuming respiration of organic matter^{4,28}. Changing wind fields may also have the potential to both increase and decrease ocean oxygen supply. For example, the continued strengthening of the Southern Ocean westerlies^{23,29} has contributed to increased formation rates of oxygen-rich intermediate water masses, which according to models may enhance global ocean oxygen supply³⁰. Conversely, the strengthening of the Pacific trade winds since the 1990s^{24,31} has led to intensified wind-driven nutrient upwelling, greater biological activity, and consequently increased O₂ consumption below the surface ocean³².

Despite recent advances in understanding the drivers of regional O₂ changes, our present understanding of the spatial distribution of O₂ changes and their causes remains limited, partly due to the superposition of a number of forcings and mechanisms that complicate clear attribution³³. While climate change is known to affect ocean oxygen by modifying wind fields and air-sea heat and freshwater fluxes²⁷, the quantitative contribution of these factors to ocean deoxygenation remains poorly constrained in observations. Observations do not allow to separate the effect of the different drivers of oxygen changes, i.e., changing wind fields and changing heat and freshwater fluxes. Also, oxygen measurements in the deep ocean are sparse and gridded observation-based data products typically provide O₂ estimates only to depths of 1000 m³⁴ or 2000 m³⁵, leaving oxygen dynamics below this depth poorly constrained.

One way to quantify the contribution of each driver and to deconstruct the superimposed mechanisms is the use of global ocean biogeochemistry models (GOBMs) run under historical atmospheric forcing. GOBMs have been shown to underestimate observationally estimated deoxygenation in the upper 700 m in the past two decades, attributed to their typical spin-up procedure that uses present-day atmospheric forcing also for pre-industrial conditions. This spin-up

procedure leads to an overly warm ocean at the beginning of the hindcast period, resulting in an underestimation of the transient ocean heat uptake³⁶ and associated deoxygenation³⁷. While this spin-up bias does not exist in fully coupled earth system models (ESMs), ESMs do not have the same phasing of the internal climate variability as observed, so the simulated interannual variability of oxygen changes also differs from reality. Also, ESMs are typically run at low resolution^{38,39}, which limits their ability to capture the effects of mesoscale eddies. Thus, despite the spin-up bias, GOBMs remain the only tool that allows isolating the role of different components of atmospheric forcing in driving historical regional and decadal changes in oxygen, albeit their underestimation of deoxygenation trends over the last two decades.

In this study, we investigate the interannual to decadal variability of O₂ over the period 1967–2018 using a GOBM at 0.25° horizontal resolution, run under historical atmospheric forcing. To isolate the effects of changing wind stress and air-sea heat and freshwater fluxes on ocean O₂, we perform a set of hindcast and sensitivity experiments run under different atmospheric forcing (see Methods). We identify the key drivers that have contributed to a sustained negative trend in the global oceanic oxygen inventory over recent decades. This trend is primarily due to changes in air-sea heat and freshwater fluxes, which affect gas solubility, ocean circulation, and ocean interior residence times. Although an increase in wind stress has led to increased ocean ventilation, particularly in the Southern Ocean, this only partially offsets the overall deoxygenation trend. Given the importance of recent changes in wind stress in mitigating global deoxygenation, a slowdown in wind stress intensification, as predicted by Earth system models^{23,40}, may accelerate ocean deoxygenation in the coming decades.

Results

Trends in the simulated global ocean oxygen inventory

The simulated trajectory of the global oceanic oxygen inventory from 1967 to 2018 can be separated into three major periods (Fig. 1a, Supplementary Table 1). In the first period, from 1967 to 1994, the global O₂ inventory gradually decreases at a rate of $-46.4 (\pm 5.0)$, standard error of the estimated linear slope) Tmol O₂ per decade (hereafter Tmol dec⁻¹). In the second period, from 1994 to 2002, the simulated trend in the O₂ inventory departs from the long-term declining trend, first falling anomalously fast until 1998 and then recovering rapidly until 2002. From 2002 to the end of the simulation period (2018), the simulated global oceanic oxygen inventory decreases continuously at an accelerated rate of -116.8 ± 6.6 Tmol dec⁻¹.

Ocean deoxygenation varies considerably with depth. Between 1967 and 1994, virtually all deoxygenation occurred in the upper 1000 m, as can be seen by comparing Fig. 1 (total water column O₂ changes) and Fig. 2 (top 1000 m O₂ changes), and as shown in Supplementary Table 2. Likewise, the transient low in the global oceanic O₂ inventory between 1994 and 2002 was also almost entirely confined to the upper 1000 m and thus left deeper layers unaffected (Supplementary Table 2). From 2002 to 2018, both depth layers, above and below 1000 m, experienced a decrease in oxygen levels, with 34% of this loss occurring in the upper 1000 m and 66% below 1000 m (Supplementary Table 2). According to these model results, deeper waters are only recently affected by deoxygenation and have been left unchanged far longer than the first 1000 m.

We further decompose O₂ changes into changes in O₂ saturation, O₂^{sat} (i.e., the thermodynamic component driven by changes in solubility), and the remaining oxygen changes, which are not driven by changes in solubility but by changes in circulation and biological activities (see Methods). Globally, solubility and non-solubility-driven changes tend to co-evolve to first order (Fig. 1), but their relative contributions to the total oxygen change differ in time (Fig. 1) and with depth (Fig. 3). From the late 1960s to the late 1990s, non-solubility effects accounted for virtually all of the deoxygenation (Fig. 1b, c). Afterward, the model suggests that non-solubility-driven and

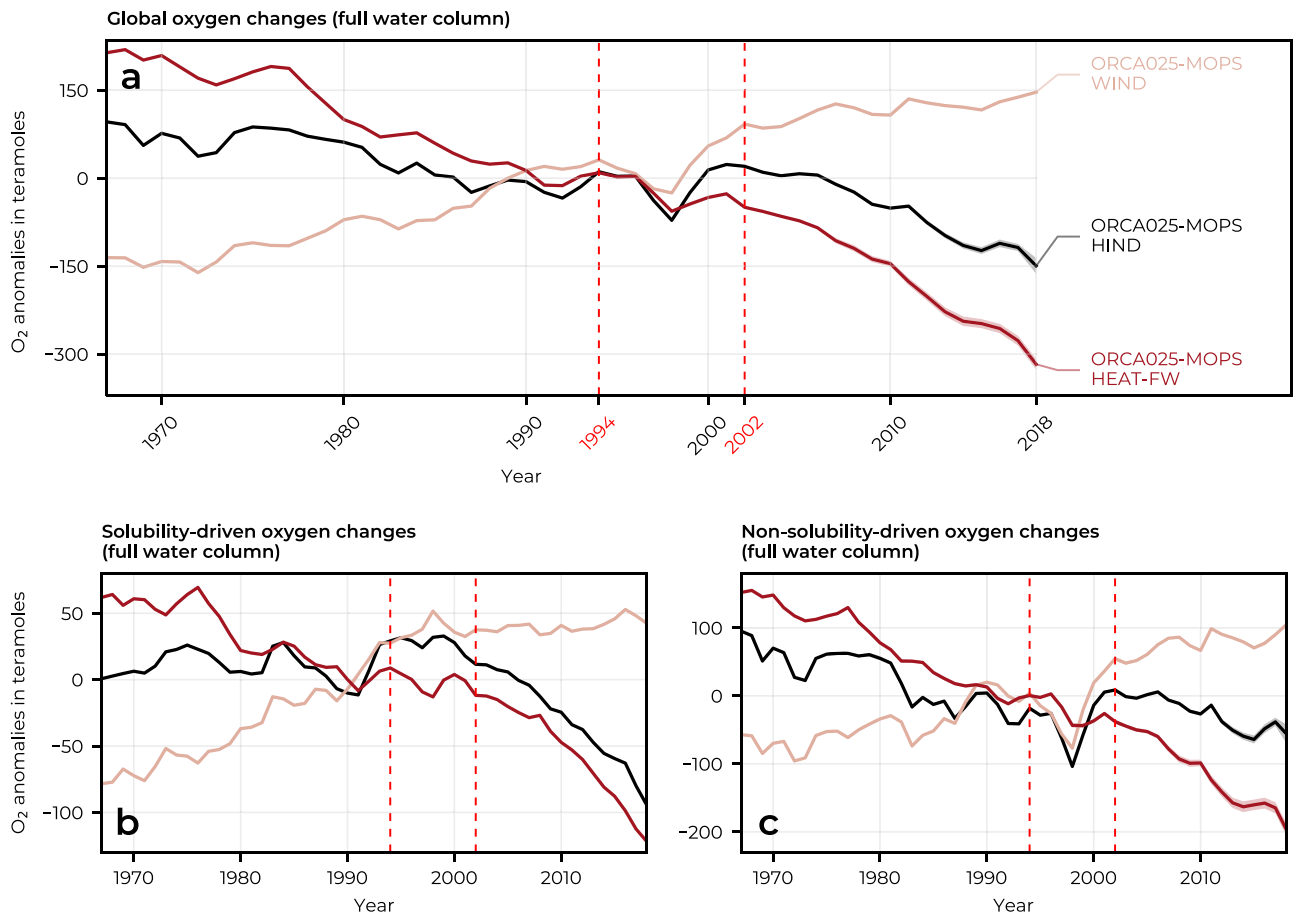


Fig. 1 | Change in the global oceanic oxygen inventory in the hindcast and sensitivity experiments. Globally integrated time series (1967–2018) of a oxygen inventory anomalies, b O₂^{sat} anomalies, and c the residual between a and b, i.e., non-solubility-driven changes, for the HIND (black), WIND (rose), and HEAT-FW (red) experiments (see Methods). The lines represent averages over the two sets of experiments (see Methods), with the shading indicating the range between the

minimum and maximum estimates. No uncertainty has been computed for the O₂^{sat} anomalies in b, as each pair of experiments share the same physics and do not differ in their O₂^{sat} estimates. All data are mean-centred using the 1967–2018 long-term mean. Red dashed vertical lines delineate the three periods of the oxygen inventory trajectory described in the results section. Note the different y-axis scales in the different panels. Source data are provided as a Source Data file.

solubility-driven changes each contribute about half of the global oxygen depletion. This shift from predominantly non-solubility-driven deoxygenation to a roughly equal contribution from solubility is consistent with observation-based estimates (Supplementary Table 3). This change coincides with an acceleration of the rise in global Ocean Heat Content (OHC), although the model underestimates this increase, as discussed in the following section. The highest rate of solubility-driven deoxygenation occurs within the upper 300 m of the water column (Fig. 3e), with non-solubility-driven changes becoming dominant below the thermocline in the model (Fig. 3i).

The simulated non-solubility-driven part of the global O₂ decrease is mainly due to changes in ocean stratification and ventilation rather than changes in remineralisation. In our simulations, remineralisation rates gradually decrease throughout the deoxygenation period 1967–2018 (Supplementary Fig. 1), indicating a slight reduction in respiratory oxygen consumption rather than an increase. The overriding importance of ventilation changes in the non-solubility-driven part of global deoxygenation is consistent with projections from an Earth system model (1990s–2090s, RCP8.5), which show that a decrease in subduction contributes to a deoxygenation trend that outweighs the mitigating effect of reduced respiration⁴¹.

Comparison to observation-based estimates of oxygen

We compare the simulated global O₂ inventory with observation-based gridded data products of ocean oxygen, which use statistical and

machine learning methods to interpolate for data gaps in space and time. Specifically, we use data from Ito et al.³⁴ (Ito-17), T. Ito, 2022⁴² (Ito-22), and GOBAI-O₂^{35,43}. The time course of the simulated global O₂ inventory of the surface ocean down to 1000 m depth is similar to the observation-based estimates Ito-17 and Ito-22 from 1967 to 1994 (Fig. 2a, Supplementary Table 4). In the mid-1990s, both simulated and observation-based estimates show a dip in the global oxygen inventory, albeit with a slightly different temporal phasing (Fig. 2a). Substantial discrepancies are found after 2002 between the observation-based and simulated estimates (Fig. 2a, Supplementary Table 4). After 2002, the observation-based data products Ito-17, Ito-22, and GOBAI-O₂ show a strong decrease in oceanic O₂, which far exceeds the deoxygenation rate observed between 1967 and 1994. In contrast, the model simulates a nearly stagnant global oceanic oxygen inventory for the upper 1000 m after 2002.

The misrepresentation of present-day deoxygenation in the model has been attributed to the spin-up procedure used by most GOBMs⁴⁴, including this study. The reduced sensitivity to global warming (Supplementary Fig. 2) leads to an underestimation of OHC increase³⁶ and of the closely-linked deoxygenation³⁷. This issue is prevalent not only in the model analysed here, but also in the GOBMs participating in RECCAP2⁴⁵ (Fig. 4), which contribute largely to the Global Ocean Carbon Budget⁴⁶. The discrepancy between modelled and observationally estimated deoxygenation after 2002 due to the biased spin-up is evident in the misrepresentation of both solubility-

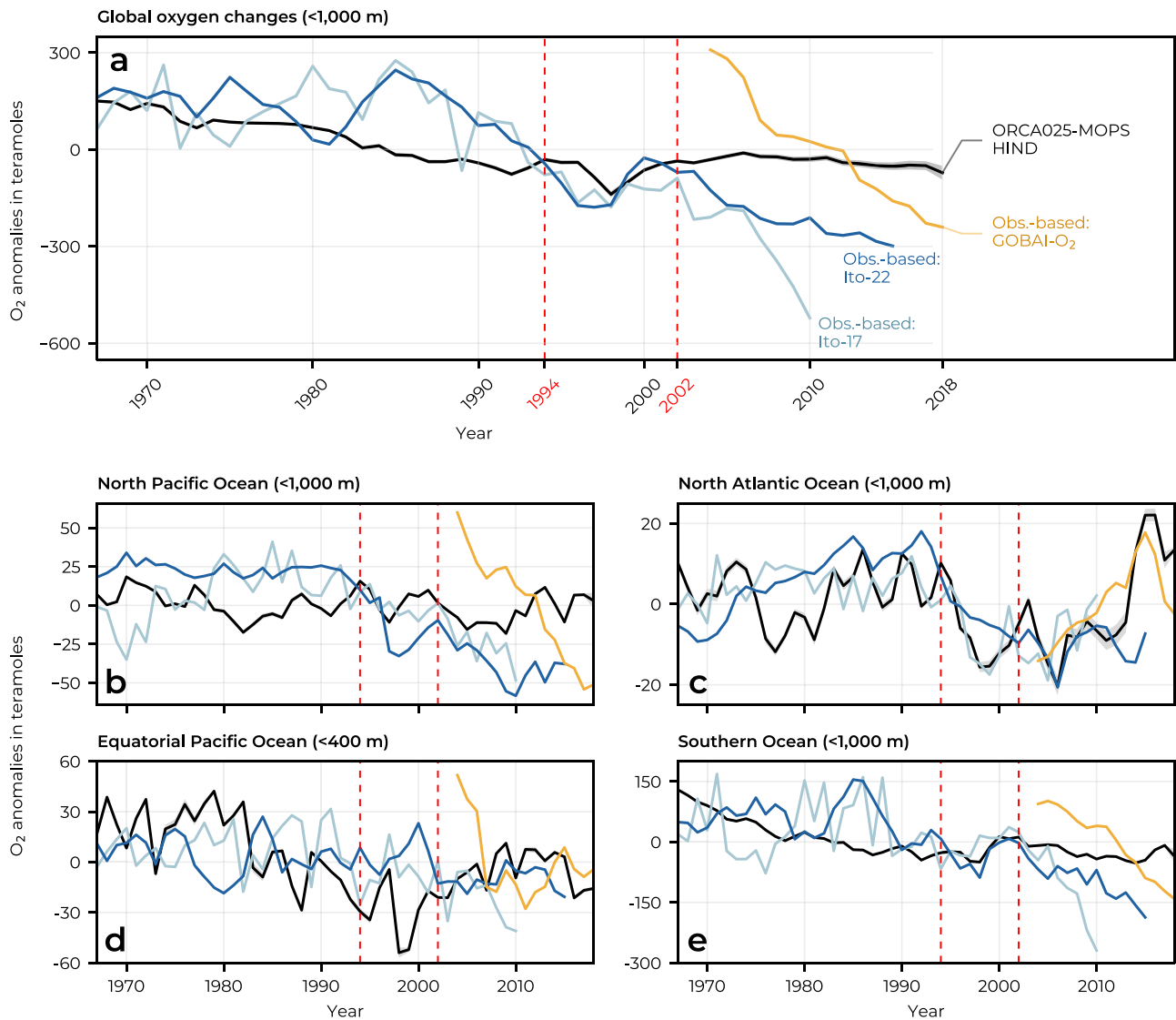


Fig. 2 | Change in global and regional oceanic oxygen inventories in the hind-cast experiment and comparable observation-based data. Time series (1967–2018) of a globally integrated upper 1000 m oceanic oxygen inventory anomalies simulated by ORCA025-MOPS HIND (black) and observation-based data from Ito-17³⁵ (light blue), Ito-22⁴³ (dark blue), and GOBAI-O₂⁴⁴ (yellow). For the model data, averages over the two sets of experiments (see Methods) are shown, with the shading indicating the range between the minimum and maximum estimate. No uncertainty estimate is reported for Ito-17³⁵. GOBAI-O₂ includes uncertainty estimates from measurement, gridding and algorithmic sources⁴⁴. Ito-22

includes uncertainty estimates from mapping errors, unresolved small-scale and high-frequency variability⁴³. These uncertainties are not comparable to the uncertainties of our model estimates and are therefore not shown. For each dataset, the data are mean-centred using the long-term mean calculated over the time span plotted. **b–e** show the same as **a**, but for four sub-regions (Supplementary Fig. 9). Red dashed vertical lines delineate the three periods of the oxygen inventory trajectory described in the results section. Note the different y-axis scales in the different panels. Source data are provided as a Source Data file.

driven (down to 2000 m depth) and non-solubility-driven (down to 400 m depth) components (Supplementary Fig. 3).

In both the Schmidtko et al.² and EN4 datasets, solubility-driven deoxygenation spreads deeper into the water column, reaching ~2000 m depth. This deep solubility-driven deoxygenation is not captured by the model and accounts for the majority of the bias. Non-solubility-driven processes, primarily ventilation, contribute less to the bias, consistent with the simulated mixed layer depth being overestimated rather than underestimated (Supplementary Fig. 4). During the well-simulated period 1967–1994, both solubility-driven and non-solubility-driven components of the O₂ trend agree well with observation-based estimates (Supplementary Fig. 5), with a notable exception: Ito-22 shows substantial non-solubility-driven deoxygenation also in the 1700–5000 m depth range (Fig. 3i) throughout the

simulation period (1967–2018), mainly in the Southern Ocean, as shown in Supplementary Fig. 6. This trend is not captured by the model, but the observation-based estimates should be treated with caution due to the paucity of deep-ocean oxygen measurements, especially in the Southern Ocean.

While the model underestimates deoxygenation in the upper 1000 m of the water column between 2002 and 2018, Fig. 2a shows that also the observation-based data products suffer from substantial uncertainties. These data products differ greatly in their estimated deoxygenation rates, with GOBAI-O₂ estimating a rate almost three times higher than that of Ito-22 (Supplementary Table 4) and highlights the need to consider the inherent uncertainties also in observation-based products when evaluating model performance⁴⁷.

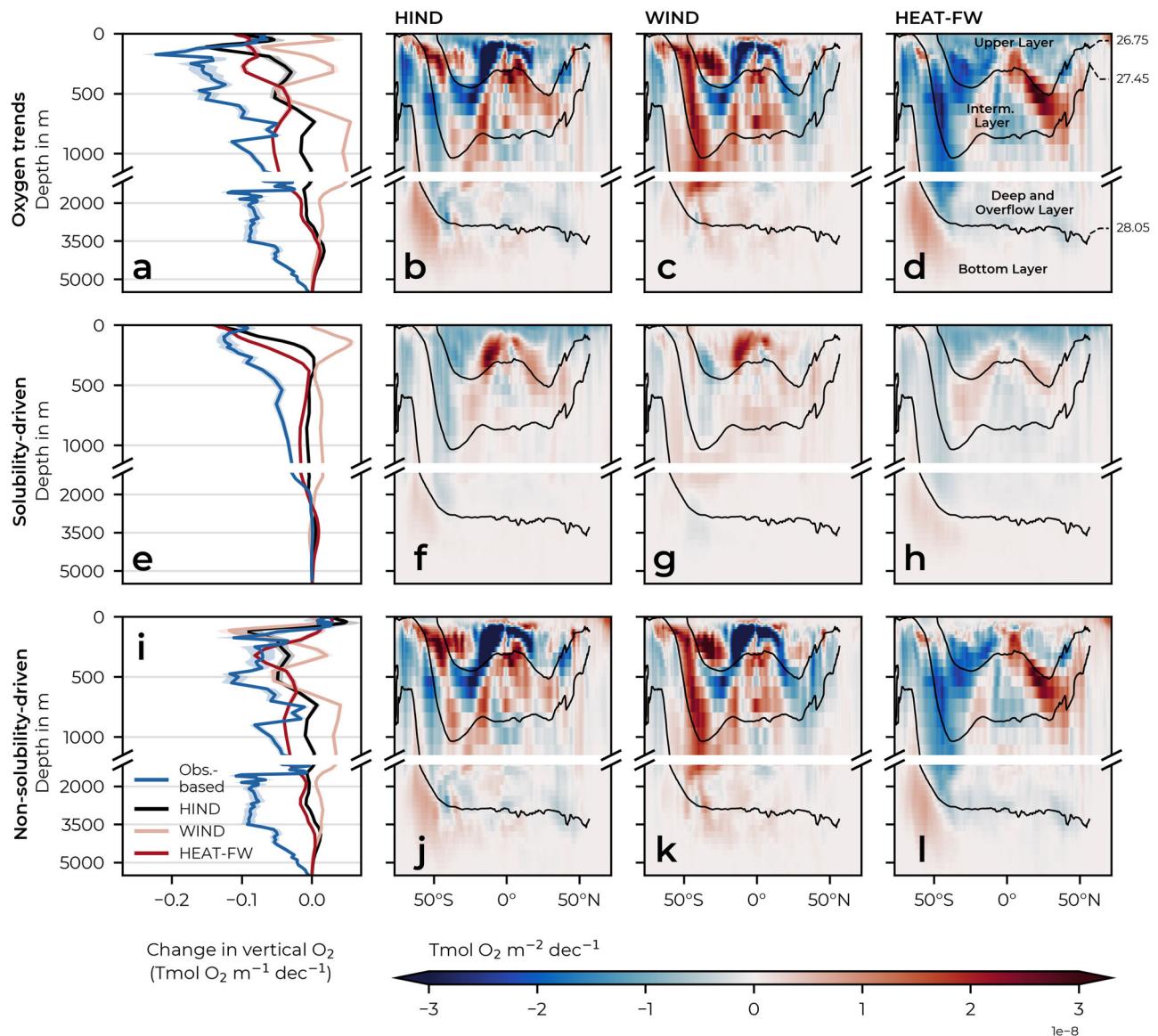


Fig. 3 | Trends in ocean oxygen by depth and latitude. Panels **a–d** show linear trends (1967–2018) in oxygen content as a function of **a** depth and **b–d** as a function of depth and latitude. The panels below show the same as **a–d**, but decompose the oxygen change into its **e–h** solubility-driven (O_2^{sat}) and **i–l** non-solubility-driven components. Trends are shown for HIND, the sensitivity experiments WIND and HEAT-FW (see Methods), and for the observation-based data products Ito-22⁴³ for

oxygen (1967–2015) and EN4.2.2¹⁰⁴ for O_2^{sat} (and their combination $O_2^{\text{total}} - O_2^{\text{sat}}$ to compute the non-solubility-driven component). The shading in the line graphs indicates the standard error of the estimated linear least-squares regression slopes and black contours show the neutral density surfaces $\sigma^{\theta} = 26.75, 27.45,$ and 28.05 kg m^{-3} , i.e., the approximate boundaries of the upper, intermediate, deep, and bottom layers. Source data are provided as a Source Data file.

Global drivers

The global deoxygenation since the 1970s has been driven by changes in air-sea heat and freshwater fluxes (hereafter buoyancy fluxes), while changes in wind stress have mitigated the overall oxygen loss (Fig. 1). Since 1967, air-sea buoyancy fluxes have led to an average decrease in the global oxygen inventory of $-94 \pm 3 \text{ Tmol dec}^{-1}$ (Fig. 1a, Supplementary Table 1). Of this oxygen loss, 32% is attributed to reduced solubility, and the remaining 68% is attributed to accumulation of non-solubility-driven oxygen losses (Supplementary Table 1). This global ocean oxygen depletion has been partly counteracted by a steady increase in wind stress (Supplementary Fig. 7), which has increased the global ocean O_2 inventory by about $64 \pm 2 \text{ Tmol dec}^{-1}$ since 1967 (Fig. 1a), through its effect on both oxygen solubility (Fig. 1b) and non-solubility-driven oxygen changes (Fig. 1c).

The acceleration of deoxygenation over the last two decades has been caused by a combination of smaller wind-driven O_2 increases and

acceleration of O_2 losses due to changes in air-sea heat and freshwater fluxes (Fig. 1a). Oxygen depletion imposed by changes in buoyancy fluxes nearly doubled between 2002 and 2018 compared to the period between 1967 and 1994 (Supplementary Table 1), coinciding with an increase in ocean heat uptake around 2000⁴⁸. As the model underestimates the ocean heat uptake over the last two decades, we expect this buoyancy-driven deoxygenation to be even higher in reality (Fig. 4). At the same time, although there is still some increase in ocean oxygen due to wind stress-driven processes, this increase is only about 40% the magnitude of the wind stress-driven oxygen increase estimated between 1967 and 1994 (Supplementary Table 1).

Regional estimates

Trends and variability in ocean oxygen vary across ocean regimes, reflecting the complexity and regional differences in the underlying drivers. The highest levels of O_2 short-term variability are found, for

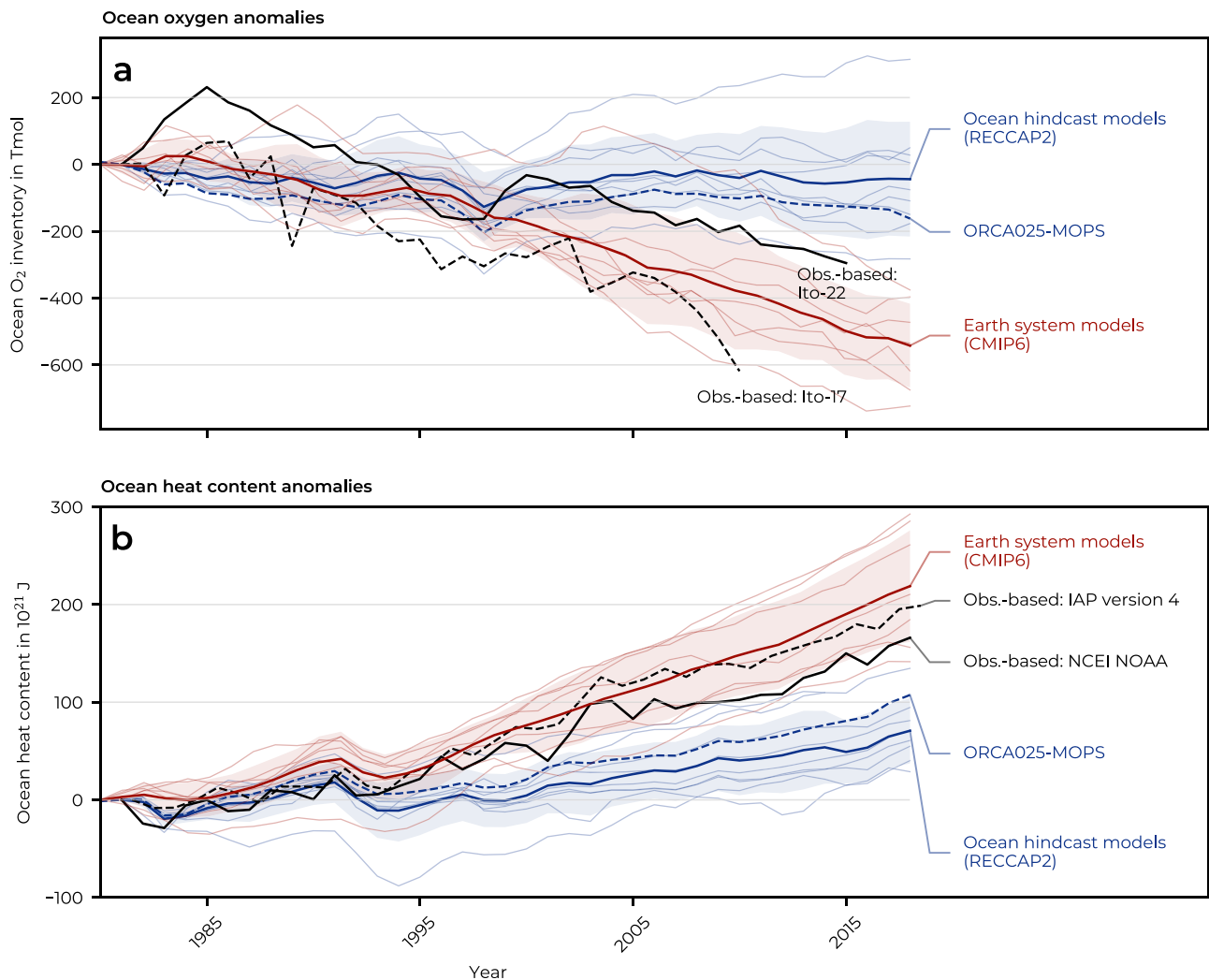


Fig. 4 | Change in ocean oxygen and ocean heat content estimated by observation-based and model-derived datasets. Annual time series of **a** ocean oxygen and **b** ocean heat content (OHC) anomalies in the upper 700 m for different observation-based and model-derived datasets. The model-based estimates are split into estimates from ocean hindcast models (datasets associated with the RECCAP2 effort¹⁰⁷), shown in blue, and Earth system models from CMIP6^{108–115}, shown in red. For each set, the multi-model mean is shown as a bold solid line, and

the associated standard deviation is shaded. Thin coloured lines show individual model estimates, and the dashed blue line shows the ORCA025-MOPS model estimate (HIND). Observation-based data are shown in black, with ocean oxygen data sourced from Ito et al.³⁵ and T. Ito⁴³, and OHC data from the National Oceanic and Atmospheric Administration (NOAA), with data updated from Levitus et al.¹⁰⁶, and IAPv4¹⁰⁵. Anomalies are calculated with respect to 1980. Source data are provided as a Source Data file.

example, in strongly dynamic regions of water mass formation, strong ocean currents, and ocean-sea ice interaction (Supplementary Fig. 8). Instead, there is little variability in the centre of the subtropical gyres and in the Weddell and Ross gyres. These regional patterns of oxygen variance are effectively reproduced by the model when compared to observation-based estimates (Supplementary Fig. 8).

The spatial extent of regions of high O₂ variability in observation-based products often appears to be larger than modelled, especially in the Southern Ocean. This relatively large spatial extent results from the scarcity of observations that have to be extrapolated over large spatial scales each year. As a consequence, the O₂ values in each cell of the observational product are not always derived from observations at the same location, and the high variability regions of the observation-based product are stretched. The high-resolution model, on the other hand, correctly captures only the interannual variability at specific locations and does not need to rely on spatial extrapolation.

We find that while changes in air-sea buoyancy fluxes are the main driver of the global long-term deoxygenation trend, wind stress is the

dominant driver of the year-to-year variability of O₂ in most ocean regions (Fig. 5). Only in areas of water mass formation, such as upper ocean mode waters in the subtropical gyres (Fig. 5g), mode and intermediate waters in the mid-latitude Southern Ocean (Fig. 5g, h), and deep and bottom waters in the North Atlantic and close to Antarctica (Fig. 5i), air-sea buoyancy fluxes are the main drivers of oxygen dynamics and explain a larger part of the interannual variability. Although the air-sea buoyancy flux affected areas are small, they largely affect the interior ocean O₂, as the newly-formed water masses penetrate deep below the surface ocean.

We further analyse in more detail the oxygen inventories for four distinct regions (Fig. 2b–e, Supplementary Fig. 9): the North Pacific Ocean, the North Atlantic Ocean, the equatorial Pacific Ocean, and the Southern Ocean. By comparing these regional trends with observation-based estimates, we find that while global deoxygenation is generally underestimated, regional trends can be captured with greater accuracy (Fig. 2). In the North Atlantic, for example, the O₂ estimates from Ito-17 and GOBAI-O₂ are very similar to the O₂ time series simulated by the model after 1990 and 2010, respectively (Fig. 2c).

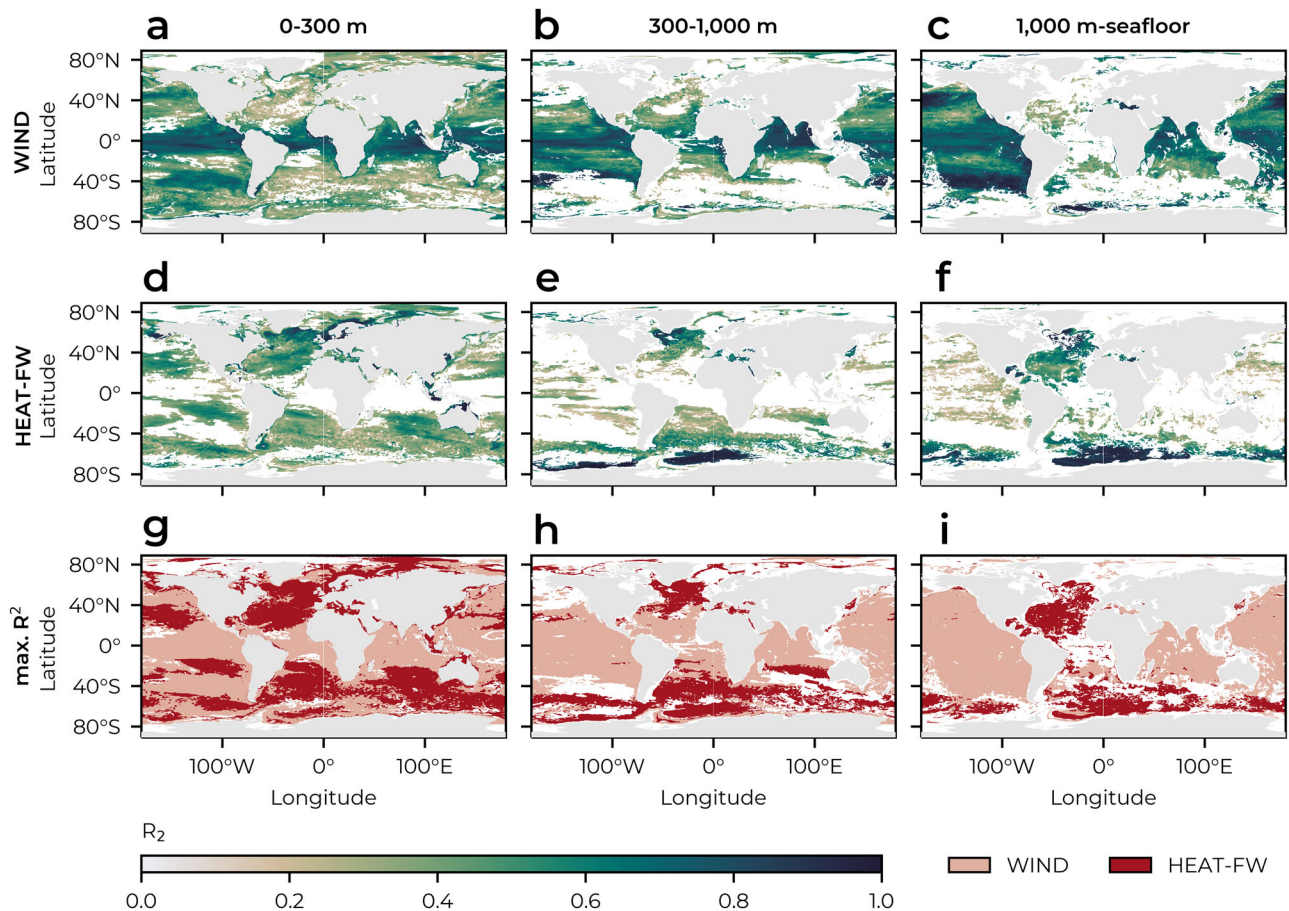


Fig. 5 | Correlation analysis between the oxygen inventory time series in the hindcast and those in the sensitivity experiments. **a–f** shows the coefficient of determination (R^2) between the oxygen inventory time series (1967–2018) in HIND and those in **a–c** WIND and **d–f** HEAT-FW (see Methods) for the three depth horizons 0–300 m, 300–1000 m, and below 1000 m (columns). Regions, where the Pearson correlation coefficient is non-significant ($p > 0.05$), are shown in white,

denoting non-significance. Based on the R^2 values, **g–i** show, for each gridpoint, whether the oxygen in HIND aligns more closely with that in WIND (rose) or HEAT-FW (red). Regions where HIND is not significantly correlated with either sensitivity experiment are shown in white. This analysis captures the relationship between the experiments on timescales from interannual to multi-decadal. Source data are provided as a Source Data file.

Owing to its large volume, Northern Hemisphere oxygen trends in the upper 1000 m (Fig. 3b) are dominated by changes in the North Pacific Ocean (Supplementary Fig. 6n). This ocean region is known for its large regional and temporal variations in dissolved oxygen, which are strongly related to the Pacific Decadal Oscillation⁴⁹. Substantial shifts in oxygen injection into the thermocline waters have been shown to result from variations in surface outcrops of different mode water masses, located primarily in the western North Pacific and affecting water masses lighter than about $\gamma^t = 26.6 \text{ kg m}^{-3}$ (generally found at depths $< 500 \text{ m}$)⁵⁰. For waters lighter than $\gamma^t = 26.6 \text{ kg m}^{-3}$, our model shows a pronounced wind stress-driven oxygen decline (Supplementary Fig. 6o), consistent with an observation-based analysis⁵¹. In addition, the buoyancy-driven simulated oxygen increase in heavier water masses (Supplementary Fig. 6p) at densities between $\gamma^t = 26.6 \text{ kg m}^{-3}$ and about $\gamma^t = 27.6 \text{ kg m}^{-3}$ (generally found at depths $< 1000 \text{ m}$) is consistent with the observation-based analysis of Mecking and Drushka⁵². Although the simulated patterns of change are consistent with previous observational studies, the simulated deoxygenation, when integrated over the entire North Pacific, is too low compared to the observation-based estimates analysed here (Fig. 2b).

In the North Atlantic basin, we find that the model captures well the decadal O_2 variability (Fig. 2c). Here, the O_2 variability is largely driven by air-sea heat fluxes and associated subpolar convective activity and MOC strength (Supplementary Fig. 10) modulated by the North Atlantic Oscillation^{53,54}. Similar to observation-based estimates,

oxygen inventories are highest in the years of high convection in the 1990s⁵⁵ and in 2014–2015⁵⁴. In depth space, we find that deoxygenation in the upper ocean is superimposed on an oxygenation trend in the intermediate and deep layers (Supplementary Fig. 6f), driven mainly by changes in buoyancy fluxes. This pattern is consistent with observation-based data⁵³ showing a deoxygenation trend between 1960–2009 in the mode and upper intermediate waters, driven by increased stratification, and an oxygenation trend in the lower intermediate waters and Labrador Seawater, driven by strong subpolar convection in the 1990s.

The equatorial regions show an overall deoxygenation that is strongest in the 100–400 m range, consistent with the observed expansion of the tropical OMZs²¹. Our findings indicate that this deoxygenation is primarily driven by wind stress-induced reductions in ventilation (Fig. 3k), predominantly originating in the Pacific Ocean (Supplementary Fig. 6). This is consistent with the concomitant weakening and shoaling of the OMZ-ventilating subtropical cells (STCs) in the model (Supplementary Fig. 11), and shown in observations⁵⁶. The shoaling of the STCs creates a pattern of deoxygenation in the 100–400 m range and oxygenation below, possibly due to the influx of more oxygenated waters. A similar pattern occurs in the Indian Ocean, and past studies have found that subsurface oxygenation has been driven by a reduction in waters supplied by the Indonesian Throughflow in favour of high-oxygen waters supplied by the Southern Indian Ocean Gyre^{57,58}.

The importance of wind stress in tropical regions, as shown in Fig. 5 and Supplementary Fig. 6b–d, is in line with previous studies showing that variations in the strength of tropical trade winds strongly influence oxygen concentrations locally^{32,59}. The large dip in O₂ in 1998, and to a lesser extent in 1983 and 2016, is consistent with the notion that during El Niño⁶⁰, shallower and less intense upwelling may reduce the upward transport of low-O₂ waters, thereby reducing the O₂ influx from the atmosphere⁵⁹. However, these dips in oxygen levels in the equatorial Pacific are not fully visible in the observational datasets analysed here (Fig. 2d).

The O₂ temporal evolution in the Southern Ocean (Fig. 2e) closely reflects that found at a global scale (Fig. 2a), showing a similar trend in the model and observation-based datasets until the early 2000s (albeit with a different phasing of the year-to-year variability) and a strong divergence thereafter. The mismatch in interannual variability in the early period may be due to the fact that the precipitation dataset before 1979 does not contain interannual variability⁶¹, and water mass transformation in the Southern Ocean is known to be driven more by freshwater than heat fluxes^{62,63}. The fact that the underestimation of global deoxygenation since 2002 is mainly due to the Southern Ocean is not surprising, since spin-up effects persist there for decades to centuries as large amounts of old water upwell in the Southern Ocean divergence zone. Similarly, the largest biases in the ocean carbon sink due to atmospheric CO₂ in the spin-up are also in the Southern Ocean⁶⁴.

At the same time, Southern Ocean observation-based estimates of deoxygenation must be interpreted with caution due to the paucity of oxygen measurements in this under-sampled region (see e.g. Supplementary Fig. 1 in ref. 35 and Fig. 1 in ref. 43). Large disagreements also exist between the trends estimated by observation-based datasets in the Southern Ocean (Fig. 2e). The differences between Ito-22 and Ito-17 can be attributed to three main factors⁴²: data sources, interpolation methods, and mapping parameters. Ito-22 relies solely on WOD bottle O₂ data, while Ito-17 combines both bottle and CTD data, resulting in different spatial coverage and data density. The restricted availability of source data, particularly in Ito-22, results in substantial data gaps that must be interpolated⁴², introducing uncertainty, especially in the under-sampled Southern Ocean. In comparison, GOBAI-O₂ uses a broader data set, including both GLODAP bottle O₂ data and Argo float measurements, and employs machine learning techniques, including random forest regression and feed-forward neural networks, for data set development⁴³. The large discrepancies in the Southern Ocean, therefore, likely reflect the sensitivity of these observation-based datasets to different data sources and the challenges of interpolation in poorly sampled regions such as the Southern Ocean.

The paucity of oxygen measurements in the Southern Ocean also casts doubt on the accuracy of the representation of interannual oxygen changes in observation-based datasets, given the high agreement between model and observation-based estimates in a very well-sampled region such as the North Atlantic^{34,42} (Fig. 2b). The accuracy of observation-based estimates of interior O₂ changes in the Southern Ocean is likely low, given that even observation-based estimates of the air-sea CO₂ flux, which are based on a larger number of surface ocean observations than estimates of interior O₂ change, have also been shown to overestimate variability in the Southern Ocean⁶⁵ as well as trends⁶⁶. Due to the shortcomings of model and observation-based estimates of O₂ inventory changes in the Southern Ocean, we cannot conclude with certainty whether model or observation-based estimates are closer to the true O₂ inventory changes in this ocean basin.

The wind stress-driven oxygenation trend found at a global scale (Fig. 1a) can be predominantly traced back to non-solubility-driven oxygenation at intermediate depths in the Southern Ocean (Fig. 3k). A steady strengthening of the Southern Hemisphere westerly winds in past decades^{59,67} is thought to have strengthened the upper cell of the MOC⁶⁸ and to have increased the ventilation of Subantarctic Mode

Water and Antarctic Intermediate Water^{69–71}. In our model results, the upper cell of the Southern Ocean MOC also shows a long-term strengthening (Supplementary Fig. 11), much of which is attributed to the wind stress strengthening (Supplementary Fig. 7). Wind stress-driven oxygenation at intermediate levels has partly been counteracted by concomitant changes in air-sea heat and freshwater fluxes that have reduced ventilation⁷¹, likely leading to ventilation-driven deoxygenation at intermediate depths of the Southern Ocean (Fig. 3l).

Discussion

In this study, we performed a set of sensitivity experiments with a high-resolution GOBM to decompose the contributions of air-sea heat freshwater fluxes and wind stress to global and regional patterns of oxygen changes. This series of experiments allowed us to identify the underlying drivers of a persistent negative trend in the global oceanic oxygen inventory since the late 1960s. We found that the overall oceanic deoxygenation was driven by changes in air-sea heat and freshwater fluxes, and was only partially counteracted by a concomitant wind stress-driven increase in ocean ventilation, mainly originating in the Southern Ocean.

While the model is generally consistent with observation-based oxygen trends until the early 2000s, the severity of observationally estimated deoxygenation from 2002 to 2018 is underestimated by a factor of about 10 compared to both Ito-17 and GOBAI-O₂, and by a factor of about 4 compared to Ito-22. We found that biases in O₂^{sat} drive most of the deoxygenation bias in the model (Supplementary Fig. 3), while non-solubility-driven processes, chiefly ventilation, contribute less to the deoxygenation bias. A large fraction of the missing global deoxygenation in the model after 2002 originates in the Southern Ocean (Fig. 2). However, determining the precise magnitude of this underestimation is complicated by substantial uncertainties also in the observation-based data products (Fig. 2). This situation highlights the need to increase both the temporal and spatial coverage of oxygen measurements, ultimately strengthening the robustness of the essential observation-based oxygen data products. This is particularly important in the Southern Ocean, where oxygen measurements are scarce, but the region is key to global oxygen dynamics.

The misrepresentation of present-day deoxygenation, a common deficiency in state-of-the-art ocean models³⁷, has been attributed to the spin-up procedure used by most GOBMs (including this study), which results in reduced sensitivity to global warming, underestimated OHC rise³⁶ and associated deoxygenation³⁷. This bias is particularly strong after 2000, which may be due to a stronger rise in the OHC after the 1990s, which is not accurately reproduced by the model (Fig. 4), especially at intermediate depths where the model is already overly warm (Supplementary Fig. 2). This discrepancy may result in less accurate simulations of oxygen trends in upwelling regions (Supplementary Fig. 12), because intermediate and deep waters have absorbed too much heat already during the spin-up phase and can therefore absorb less heat in the last 1958–2018 cycle. Conversely, and as also reported by Takano et al.³⁷, coupled Earth System Models (ESMs) from CMIP6, which often share the ocean components with GOBMs, simulate upper 700 m deoxygenation and ocean warming trends that are consistent with observation-based estimates within uncertainties (Fig. 4). Future modelling studies should adjust the forcing fields used during spin-up to be more representative of pre-industrial conditions, as successfully implemented by Huguenin et al.³⁶.

While the deoxygenation trend since the early 2000s is underestimated in the model, the trends before 2002, which are less affected by the recent OHC rise, are better captured. Also, the trends in the WIND experiment, which by construction does not capture the direct effects of global warming (but only its indirect effects manifested through wind field changes), are less biased than the trends in HEAT-FW. At a regional scale, the model performs well in capturing the regional patterns of maximum O₂ variability and the decadal O₂

variability driven by North Atlantic convection. This ability can be explained by the fact that regionally most of the O_2 variability is driven by its non-solubility component (Supplementary Fig. 13), so that the known O_2^{sat} bias does not exert a significant influence. Ventilation and convection are intimately linked to ocean circulation, which in turn is driven by wind stress and air-sea heat and freshwater fluxes. Since these processes depend critically on the ability of the model to accurately simulate the large- and small-scale circulation features⁷², we argue that high-resolution GOBMs, such as the one used here, are better suited to capture the regional patterns of O_2 changes than coarse-resolution ESMs.

A key region for global oxygen trends is the Southern Ocean, where the formation of mode and intermediate waters is a key conduit for oxygen, nutrients, and anthropogenic carbon and heat into the interior ocean^{73,74}. In this region, westerly winds have strengthened in recent decades due to increasing greenhouse gas emissions and stratospheric ozone depletion²⁹, which have been shown to have significant and distinct effects on biogeochemistry⁷⁵. Our results suggest that the wind strengthening has counteracted the deoxygenation caused by widespread surface warming and mid-depth freshening^{76,77}. The poleward shift and implicit movement of the sinking branch of intermediate water masses into denser water may have further accelerated intermediate water mass formation⁶⁸, while increasing oxygen solubility in subsided waters. By modulating the strength of the Southern Ocean upper circulation cell⁶⁸ and setting the formation rates and regions of oxygen-rich intermediate water masses^{70,71}, the Southern Hemisphere westerly winds are critical for global oxygen supply³⁰.

Recent studies suggest that the current intensification of westerlies in the Southern Hemisphere may slow or cease altogether in the coming century under low to moderate emissions scenarios that align with or approach the temperature targets of the Paris Agreement^{23,40}. In these scenarios, the slowdown in wind stress intensification and the concomitant vanishing of wind-driven oxygen enrichment is attributed to the recovery of stratospheric ozone by mid-century⁷⁸. The reduction in ventilation-driven oxygen supply under these low emissions scenarios is likely to coincide with additional losses caused by ocean warming, even if CO_2 emissions are stopped^{79–81}. The ocean will continue to warm to equilibrate with the warmer atmosphere and thus continue to lose oxygen^{6,82,83}. Our study raises the question of whether the stabilisation or reversal of the past intensification of wind stress, together with continued ocean warming, will accelerate oxygen loss in the future, particularly in the Southern Hemisphere intermediate waters and in regions fed by these water masses, such as the equatorial OMZs⁸⁴.

Our analysis demonstrates the complex interplay between the counteracting forces of wind stress and air-sea heat and freshwater fluxes, emphasising their importance in determining changes in oceanic oxygen. Given the centrality of atmospheric drivers in influencing oceanic oxygen trends, we stress the importance of accurately representing wind stress and air-sea heat and freshwater fluxes in reanalysis data, including pre-industrial conditions used during spin-up to assess past deoxygenation with GOBMs. In addition, a robust projection of wind stress and air-sea heat and freshwater fluxes in coupled ESMs is essential for a robust prediction of future changes in O_2 and OHC. This analysis identifies the drivers of deoxygenation and their regional patterns. It contributes to a much-needed improved mechanistic understanding of O_2 changes, critical to better predict and anticipate future global and regional O_2 inventory changes and their potential consequences for marine ecosystems.

Methods

ORCA025-MOPS model

We used a global configuration of the ocean-sea ice model NEMO-LIM2⁸⁵ with a horizontal resolution of 0.25° (ORCA025) and 46

unequally spaced vertical levels that increase with depth⁸⁶. The model resolution is sufficient to capture much of the mesoscale eddy spectrum⁸⁷, so no eddy parameterisation was used. The ocean-sea ice model was coupled to the marine biogeochemical model MOPS^{88,89}, which simulates the lower trophic levels of the ecosystem and the associated nutrient cycling using nine tracers: phosphate (P), nitrate (N), O_2 (O), dissolved inorganic carbon, alkalinity, and fixed-stoichiometry representations of phytoplankton, zooplankton, detritus, and dissolved organic matter. We find that the choice of biogeochemical parameters, and in particular the stoichiometric $O_2:P$ ratio, can influence the long-term trends and adjustment times of ocean oxygen^{88,90}. To evaluate the uncertainty associated with the choice of the $O_2:P$ ratio, we employ two different model configurations with different values of the parameter ($O_2:P$ ratio of either 150 or 162).

ORCA025-MOPS was initialised by a spin-up performed with the 0.5° resolution model ORCA05-MOPS. ORCA05-MOPS was initialised with climatological temperature and salinity from Levitus98⁹¹, with World Ocean Atlas 2013 conditions^{92,93} for PO_4 , NO_3 , and O_2 , and with GLODAPv2 conditions⁹⁴ for alkalinity and C_{nat} (pre-industrial carbon). The model was forced by the JRA55-do runoff dataset (version 1.1, at 0.25° horizontal resolution) and JRA55-do atmospheric forcing dataset (version 1.4, at 0.25° horizontal and 3-hourly temporal resolution) from 1958 to 2018⁶¹. ORCA05-MOPS was run under three cycles of JRA55-do atmospheric forcing, amounting to a total spin-up of 183 years. The end of the third cycle of ORCA05-MOPS provided the biogeochemical initial conditions for a spin-up with the 0.25° resolution model ORCA025-MOPS, run under one cycle of JRA55-do atmospheric forcing. For technical reasons, the physics had to be restarted from Levitus98. The end of the fourth cycle provided the initial conditions for the experiments analysed in this study.

Errors in the representation of biogeochemical processes in the model may bias the results, particularly in the low-oxygen zones along the eastern margins where biogeochemical processes are of high importance in altering the oxygen demand⁹⁵. It has been suggested that the temperature dependence of remineralisation may impact O_2 concentrations through shoaling of remineralisation profiles⁹⁶. In MOPS, remineralisation is temperature-independent, so these effects are neglected. The distribution of phytoplankton in the surface layer (-6 m) in ORCA025-MOPS is generally in good agreement with observation-based estimates (Supplementary Fig. 14), crucial for accurately representing remineralisation. The strongest discrepancies are found in coastal regions, where modelled phytoplankton biomass is typically below that observed (Supplementary Fig. 14), possibly due to simplifications in the representation of terrestrial nutrient runoff, including the absence of additional and increasing nutrient inputs from anthropogenic sources⁹⁷. In the pelagic ocean, modelled phytoplankton biomass is typically higher than observed (Supplementary Fig. 14), likely due to the neglect of iron limitation in the model⁸⁹. While the calibrated parameters of ORCA025-MOPS may mitigate this deficiency somewhat⁹⁰, this omission may still lead to an overestimation of primary production and concomitant remineralisation and oxygen loss below the sea surface, especially in the Southern Ocean and upwelling regions where iron is a limiting nutrient^{98,99}. Although zooplankton is less homogeneously distributed than phytoplankton, the spatial differences from observation-based estimates are similar, with both being overestimated around the equator and in the Southern Ocean at $40^\circ S$. The sparse data on zooplankton biomass, however, makes a robust assessment difficult (Supplementary Fig. 14).

Simulations

For both model configurations ($O_2:P$ ratio of 150 or 162), four experiments were run. A hindcast (HIND) experiment, performed under interannual forcing of JRA55-do, simulates changes in the O_2 inventory due to climate change and climate variability. However, HIND may also contain O_2 changes introduced by a spurious model drift, as the model

is not expected to be in equilibrium after the relatively short spin-up time compared to deep-ocean equilibration timescales. To quantify this model drift, we performed a repeated-year-forcing (RYF) experiment, which was integrated by repeating the JRA55-do forcing of a single year (1 May 1990 to 30 April 1991), most neutral in terms of the major climate modes¹⁰⁰. The RYF experiment does not include changes in the O₂ inventory due to climate change nor due to climate variability, so any ongoing changes are caused by the model drift. To correct for such model drift, the O₂ inventories in RYF were removed (gridpoint-wise and for each year) from those in HIND, under the assumption that the drifts in HIND and RYF are the same. As RYF simulates neither climate change nor climate variability, the difference between the two experiments results in O₂ inventory anomalies caused by climate change and variability only. This procedure is commonly used to differentiate between steady-state and non-steady-state components of ocean biogeochemical tracers^{45,46}, including O₂¹⁰¹. Depending on the selected value of the O₂:P ratio, the drifts in the two RYF experiments are +0.23 and -0.13 Pmol O₂ per decade (Supplementary Fig. 15a). The choice of the O₂:P ratio does not, however, substantially influence the HIND minus RYF O₂ anomalies. The O₂ anomalies are nearly identical between the two experiment twins (Supplementary Fig. 15b), suggesting that the biogeochemical parameterisation does not substantially influence the decadal climate-driven O₂ trends and variability that are the focus of this paper.

Following the strategy used in Patara et al.⁷¹, two complementary sensitivity experiments were performed to isolate the effects of changing air-sea heat and freshwater fluxes and wind stress on oxygen dynamics. In the air-sea heat and freshwater fluxes experiment (HEAT-FW), the interannual variability of the wind stress was suppressed, while the interannual variability of all variables needed to compute the air-sea fluxes of heat, freshwater, and oxygen was preserved. The opposite is true for the wind stress experiment (WIND), where only the interannual variability of wind stress was retained. The atmospheric variables used to compute the air-sea fluxes of heat, freshwater and oxygen are wind speed, air temperature, humidity, incoming solar radiation, outgoing longwave radiation, and precipitation. Similarly, RYF was subtracted from HEAT-FW and WIND to isolate the effects of interannual variability and climate change in air-sea heat and freshwater fluxes (for HEAT-FW) and in wind stress (for WIND) on oceanic O₂. In the text, HIND, HEAT-FW, and WIND refer to the average of the drift-corrected results from each of the two model configurations. Note that in all four experiments, the years 1958 to 1967 were not included in the analyses performed due to the initial shock and associated recovery phase that the model undergoes when the forcing abruptly jumps from 2018 back to 1958^{36,37,44}.

Changes in oceanic dissolved oxygen were further decomposed into two fractions for analysis of the underlying mechanisms: (1) solubility-driven changes and (2) non-solubility-driven changes (i.e., oxygen changes driven by changes in respiration or ventilation). O₂ solubility in seawater was approximated by O₂^{sat}, calculated from potential temperature and salinity¹⁰², and represents the O₂ concentration that a water mass has reached when in equilibrium with the O₂ partial pressure of the overlying atmosphere. Non-solubility-driven oxygen changes were calculated by subtracting the solubility component from the total oxygen anomaly³⁴, thereby isolating the fraction of oxygen changes that cannot be explained by solubility changes, and corresponds to the opposite of the commonly used Apparent Oxygen Utilisation (AOU) diagnostic.

Observation-based datasets

We compare the simulated oxygen trends with observation-based estimates. Specifically, we use the observation-based data products GOBAI-O₂^{35,43} (2004–2022), and oxygen concentration anomalies developed by Ito et al.^{34,42}, referred to as Ito-17 (1950–2015) and Ito-22 (1965–2015), respectively. Due to the relatively low sampling density in

Ito-17 before 1960 and after 2010³⁴, only data from 1960–2010 were used. As Ito-17 and our simulations provide O₂ anomalies, GOBAI-O₂ inventories were also converted to anomalies by subtracting the long-term mean. To compare the simulated O₂^{sat} trends with observation-based estimates, we calculate O₂^{sat} from the EN4 temperature and salinity data¹⁰³ (version EN.4.2.2).

Additionally, in Supplementary Text 2 and Supplementary Figs. 16–18 in the Supplementary Materials, we compare observation-based climatological distributions of dissolved oxygen and O₂^{sat} against the corresponding model outputs.

Further, we compare the simulated trend in global OHC with observation-based estimates. Specifically, we use the observation-based data products IAPv4¹⁰⁴, and OHC data from the National Oceanic and Atmospheric Administration (NOAA, updated from Levitus et al.¹⁰⁵).

RECCAP2 models

To compare the ORCA025-MOPS simulations with other hindcast simulations, we used nine GOBMs (CESM-ETHZ, CNRM-ESM2-1, EC-Earth3, FESOM-REcoM-LR, MOM6-Princeton, MRI-ESM2-1, NorESM-OC1.2, ORCA025-GEOMAR, and ORCA1-LIM3-PISCES) from RECCAP2^{45,106}. Only models evaluated in the model evaluation chapter of RECCAP2 were used, as the remaining models either had drift problems when branching from another simulation with coarser model resolution, had too large salinity biases, or had incomparable historical and control simulations due to their setup⁶⁴. Consistent with the analysis of ORCA025-MOPS, we calculated anomalies in OHC and O₂ by subtracting the simulation without climate change and variability from the historical simulation with climate change and variability.

CMIP6 earth system models

Additionally, we have analysed all seven ESMs from CMIP6 to compare hindcast simulations with fully coupled simulations. The ESMs used here are ACCESS-ESM1-5 (ensemble member r1i1p1f1)¹⁰⁷, CanESM5 (r1i1p1f1), and CanESM5-CanOE (r1i1p2f1)¹⁰⁸, CNRM-ESM2-1 (r1i1p1f2)¹⁰⁹, GFDL-CM4 (r1i1p1f1) and GFDL-ESM4 (r1i1p1f1)^{110–112}, and MPI-ESM1-2-LR (r1i1p1f1)^{113,114}. We used all ESM outputs for which O₂ and potential temperature were available for the historical simulation, the SSPs 5–8.5 (SSP5–8.5) simulation¹¹⁵, and the pre-industrial control simulation. The SSP5–8.5 simulations were used for the years 2015 to 2018 because the historical simulation in CMIP6 stopped after 2014. From 2015 to 2018, SSP5–8.5 was chosen because it is the pathway for which most ESMs provide results. Although it is a high-emission pathway, the radiative forcing in these years is almost identical for all SSPs in the first year, and the marginal differences in radiative forcing are too small to distinguish the climate in the first years between SSPs. Here the anomaly has been calculated as the difference between the pre-industrial control run and the historical run. As the pre-industrial run still simulates internal climate variability, this difference only quantifies the effect of climate change and externally forced variability, such as volcanoes, and not the effect of internal climate variability. The remaining internal climate variability in the anomaly is a superposition of the internal climate variability from the historical simulation and that from the pre-industrial control simulation and has no scientific relevance.

Data availability

A subset of the output data generated in this study is available through GEOMAR at <https://hdl:20.500.12085/a4d451d5-a68f-401b-b58d-68792a5a0820>¹¹⁶. All other model outputs presented here are available upon request. Source data for all figures, including Supplementary Figs., are provided with this paper and are available at the same address [<https://hdl.handle.net/20.500.12085/a4d451d5-a68f-401b-b58d-68792a5a0820>]. The Earth system model output used in this study is available via the Earth System Grid Federation [<https://esgf-node.ipsl.upmc.fr/projects/esgf-ipsl/>]. The RECCAP2 model output

used in this study is openly accessible in the Zenodo database under record number [7990823](https://zenodo.org/record/7990823). All observational data used for model evaluation are openly available to the public at the following links: Oxygen data from Ito et al.³⁴ are available at [<https://o2.eas.gatech.edu/data.html>] and from GOBAI-O₂⁴³ at [<https://doi.org/10.25921/z72m-yz67>]. Oxygen data from T. Ito⁴² are available from the Biological & Chemical Oceanography Data Management Office (BCO-DMO) at [<https://doi.org/10.26008/1912/bco-dmo.816978.1>] and [<https://www.bco-dmo.org/dataset/816978>]. EN4 temperature and salinity data¹⁰³ (version EN.4.2.2) were obtained from [<https://www.metoffice.gov.uk/hadobs/en4/>]. OHC data from NOAA are available at [<https://ncei.noaa.gov/access>] and from IAPv4¹⁰⁴ at [www.ocean.iap.ac.cn].

Code availability

The Python scripts used for all analyses and figures are available through GEOMAR at <https://hdl:20.500.12085/a4d451d5-a68f-401b-b58d-68792a5a0820>¹¹⁶.

References

- Breitburg, D. et al. Declining oxygen in the global ocean and coastal waters. *Science* **359**, eaam7240 (2018).
- Schmidtko, S., Stramma, L. & Visbeck, M. Decline in global oceanic oxygen content during the past five decades. *Nature* **542**, 335–339 (2017).
- Bindoff, N. L. et al. Changing ocean, marine ecosystems, and dependent communities. In: Pörtner, H. O. et al. (eds.) *IPCC Special Report on the Ocean and Cryosphere in a Changing Climate*, 447–587 (Cambridge University Press, Cambridge, UK and New York, NY, USA, 2019).
- Bopp, L. et al. Multiple stressors of ocean ecosystems in the 21st century: projections with CMIP5 models. *Biogeosciences* **10**, 6225–6245 (2013).
- Kwiatkowski, L. et al. Twenty-first century ocean warming, acidification, deoxygenation, and upper-ocean nutrient and primary production decline from CMIP6 model projections. *Biogeosciences* **17**, 3439–3470 (2020).
- Oschlies, A. A committed fourfold increase in ocean oxygen loss. *Nat. Commun.* **12**, 2307 (2021).
- Stramma, L. & Schmidtko, S. Spatial and temporal variability of oceanic oxygen changes and underlying trends. *Atmos. Ocean* **59**, 122–132 (2021).
- Portela, E., Kolodziejczyk, N., Vic, C. & Thierry, V. Physical mechanisms driving oxygen subduction in the global ocean. *Geophys. Res. Lett.* **47**, e2020GL089040 (2020).
- Khatiwal, S., Primeau, F. & Holzer, M. Ventilation of the deep ocean constrained with tracer observations and implications for radiocarbon estimates of ideal mean age. *Earth Planet. Sci. Lett.* **325**, 116–125 (2012).
- Morrison, A. K., Waugh, D. W., Hogg, A. M., Jones, D. C. & Abernathy, R. P. Ventilation of the Southern Ocean pycnocline. *Annu. Rev. Mar. Sci.* **14**, 405–430 (2022).
- Marshall, J. & Speer, K. Closure of the meridional overturning circulation through Southern Ocean upwelling. *Nat. Geosci.* **5**, 171–180 (2012).
- Elipot, S., Frajka-Williams, E., Hughes, C. W., Olhede, S. & Lankhorst, M. Observed basin-scale response of the North Atlantic meridional overturning circulation to wind stress forcing. *J. Clim.* **30**, 2029–2054 (2017).
- Koelling, J., Atamanchuk, D., Wallace, D. W. R. & Karstensen, J. Decadal variability of oxygen uptake, export, and storage in the Labrador Sea from observations and CMIP6 models. *Front. Mar. Sci.* **10**, 1202299 (2023).
- Lozier, M. S. Overturning in the subpolar North Atlantic: a review. *Philos. Trans. R. Soc. A: Math. Phys. Eng. Sci.* **381**, 20220191 (2023).
- Gordon, A. L. Deep antarctic convection west of Maud Rise. *J. Phys. Oceanogr.* **8**, 600–612 (1978).
- Gordon, A. L. Bottom water formation. In Steele J. H., T. K. K., Thorpe S. A. (ed.) *Ocean Currents*, 263–269 (Academic Press, London, United Kingdom, 2009).
- Hanawa, K. & Talley, L. D. Mode waters. **77**, 373–386 (Elsevier, 2001).
- Talley, L. D., Pickard, G. L., Emery, W. J. & Swift, J. H. *Descriptive physical oceanography*, 6 edn (Elsevier Science & Technology, 2011).
- Garcia, H. E. et al. World Ocean Atlas 2018, Volume 3: Dissolved oxygen, apparent oxygen utilization, and oxygen saturation. *NOAA Atlas NESDIS* **15**, 38 pp. (2019).
- Luyten, J. R., Pedlosky, J. & Stommel, H. The ventilated thermocline. *J. Phys. Oceanogr.* **13**, 292–309 (1983).
- Stramma, L., Johnson, G. C., Sprintall, J. & Mohrholz, V. Expanding oxygen-minimum zones in the tropical oceans. *Science* **320**, 655–658 (2008).
- von Schuckmann, K. et al. Heat stored in the Earth system: where does the energy go? *Earth Syst. Sci. Data* **12**, 2013–2041 (2020).
- Goyal, R., Sen Gupta, A., Jucker, M. & England, M. H. Historical and projected changes in the Southern Hemisphere surface westerlies. *Geophys. Res. Lett.* **48**, e2020GL090849 (2021).
- Yang, F., Zhang, L. & Long, M. Intensification of Pacific trade wind and related changes in the relationship between sea surface temperature and sea level pressure. *Geophys. Res. Lett.* **49**, e2022GL098052 (2022).
- Helm, K. P., Bindoff, N. L. & Church, J. A. Observed decreases in oxygen content of the global ocean. *Geophys. Res. Lett.* **38**, L23602 (2011).
- Li, G. et al. Increasing ocean stratification over the past half-century. *Nat. Clim. Change* **10**, 1116–1123 (2020).
- Oschlies, A. Ocean deoxygenation from climate change. In: Laffoley, D. & Baxter, J. M. (eds.) *Ocean deoxygenation: everyone's problem - causes, impacts, consequences and solutions*, 105–116 (Gland, Switzerland: IUCN, 2019).
- Bopp, L. et al. Potential impact of climate change on marine export production. *Glob. Biogeochem. Cycles* **15**, 81–99 (2001).
- Thompson, D. W. J. et al. Signatures of the Antarctic ozone hole in Southern Hemisphere surface climate change. *Nat. Geosci.* **4**, 741–749 (2011).
- Getzlaff, J., Dietze, H. & Oschlies, A. Simulated effects of southern hemispheric wind changes on the Pacific oxygen minimum zone. *Geophys. Res. Lett.* **43**, 728–734 (2016).
- de Boissésón, E., Balmaseda, M. A., Abdalla, S., Källén, E. & Janssen, P. A. E. M. How robust is the recent strengthening of the Tropical Pacific trade winds? *Geophys. Res. Lett.* **41**, 4398–4405 (2014).
- Ridder, N. N. & England, M. H. Sensitivity of ocean oxygenation to variations in tropical zonal wind stress magnitude. *Glob. Biogeochem. Cycles* **28**, 909–926 (2014).
- Oschlies, A., Brandt, P., Stramma, L. & Schmidtko, S. Drivers and mechanisms of ocean deoxygenation. *Nat. Geosci.* **11**, 467–473 (2018).
- Ito, T., Minobe, S., Long, M. C. & Deutsch, C. Upper ocean O₂ trends: 1958–2015. *Geophys. Res. Lett.* **44**, 4214–4223 (2017).
- Sharp, J. D. et al. GOBAI-O₂: A global gridded monthly dataset of ocean interior dissolved oxygen concentrations based on shipboard and autonomous observations [dataset] (2022). NCEI Accession O259304 (2023).
- Huguenin, M. F., Holmes, R. M. & England, M. H. Drivers and distribution of global ocean heat uptake over the last half century. *Nat. Commun.* **13**, 4921 (2022).

37. Takano, Y. et al. Simulations of ocean deoxygenation in the historical era: insights from forced and coupled models. *Front. Mar. Sci.* **10**, 1139917 (2023).
38. Beadling, R. L. et al. Representation of Southern Ocean properties across coupled model intercomparison project generations: CMIP3 to CMIP6. *J. Clim.* **33**, 6555–6581 (2020).
39. Terhaar, J., Frölicher, T. L. & Joos, F. Observation-constrained estimates of the global ocean carbon sink from Earth system models. *Biogeosciences* **19**, 4431–4457 (2022).
40. Deng, K. et al. Changes of Southern Hemisphere westerlies in the future warming climate. *Atmos. Res.* **270**, 106040 (2022).
41. Couespel, D., Lévy, M. & Bopp, L. Major contribution of reduced upper ocean oxygen mixing to global ocean deoxygenation in an earth system model. *Geophys. Res. Lett.* **46**, 12239–12249 (2019).
42. Ito, T. Optimal interpolation of global dissolved oxygen: 1965–2015. *Geosci. Data J.* **9**, 167–176 (2022).
43. Sharp, J. D. et al. GOBAL-O₂: temporally and spatially resolved fields of ocean interior dissolved oxygen over nearly two decades. *Earth Syst. Sci. Data* **15**, 4481–4518 (2023).
44. Tsujino, H. et al. Evaluation of global ocean-sea-ice model simulations based on the experimental protocols of the Ocean Model Intercomparison Project phase 2 (OMIP-2). *Geosci. Model Dev.* **13**, 3643–3708 (2020).
45. DeVries, T. et al. Magnitude, trends, and variability of the global ocean carbon sink from 1985 to 2018. *Glob. Biogeochem. Cycles* **37**, e2023GB007780 (2023).
46. Friedlingstein, P. et al. Global carbon budget 2023. *Earth Syst. Sci. Data* **15**, 5301–5369 (2023).
47. Ito, T. et al. Underestimation of multi-decadal global O₂ loss due to an optimal interpolation method. *Biogeosciences* **21**, 747–759 (2024).
48. Cheng, L. et al. Past and future ocean warming. *Nat. Rev. Earth Environ.* **3**, 776–794 (2022).
49. Duteil, O., Oschlies, A. & Böning, C. W. Pacific Decadal Oscillation and recent oxygen decline in the eastern tropical Pacific Ocean. *Biogeosciences* **15**, 7111–7126 (2018).
50. Kwon, E. Y., Deutsch, C., Xie, S.-P., Schmidtko, S. & Cho, Y.-K. The North Pacific oxygen uptake rates over the past half century. *J. Clim.* **29**, 61–76 (2016).
51. Deutsch, C., Emerson, S. & Thompson, L. Physical-biological interactions in North Pacific oxygen variability. *J. Geophys. Res. Oceans* **111**, C09S90 (2006).
52. Mecking, S. & Drushka, K. Linking northeastern North Pacific oxygen changes to upstream surface outcrop variations. *Biogeosciences* **21**, 1117–1133 (2024).
53. Stendardo, I. & Gruber, N. Oxygen trends over five decades in the North Atlantic. *J. Geophys. Res. Oceans* **117**, C11004 (2012).
54. Koelling, J., Wallace, D. W. R., Send, U. & Karstensen, J. Intense oceanic uptake of oxygen during 2014–2015 winter convection in the Labrador Sea. *Geophys. Res. Lett.* **44**, 7855–7864 (2017).
55. Böning, C. W. et al. Decadal changes in Atlantic overturning due to the excessive 1990s Labrador Sea convection. *Nat. Commun.* **14**, 4635 (2023).
56. Farneti, R., Dwivedi, S., Kucharski, F., Molteni, F. & Griffies, S. M. On Pacific subtropical cell variability over the second half of the twentieth century. *J. Clim.* **27**, 7102–7112 (2014).
57. Ditkovsky, S., Resplandy, L. & Busecke, J. Unique ocean circulation pathways reshape the Indian Ocean oxygen minimum zone with warming. *Biogeosciences* **20**, 4711–4736 (2023).
58. Roach, C. J. & Bindoff, N. L. Developing a new oxygen atlas of the world's oceans using data interpolating variational analysis. *J. Atmos. Ocean. Technol.* **40**, 1475–1491 (2023).
59. Eddebbar, Y. A. et al. Impacts of ENSO on air-sea oxygen exchange: observations and mechanisms. *Glob. Biogeochem. Cycles* **31**, 901–921 (2017).
60. Wolter, K. & Timlin, M. S. El Niño/Southern Oscillation behaviour since 1871 as diagnosed in an extended multivariate ENSO index (MEI.ext). *Int. J. Climatol.* **31**, 1074–1087 (2011).
61. Tsujino, H. et al. JRA-55 based surface dataset for driving ocean-sea-ice models (JRA55-do). *Ocean Model.* **130**, 79–139 (2018).
62. Karstensen, J. & Lorbacher, K. A practical indicator for surface ocean heat and freshwater buoyancy fluxes and its application to the NCEP reanalysis data. *Tellus A: Dyn. Meteorol. Oceanogr.* **63**, 338–347 (2011).
63. Terhaar, J., Frölicher, T. L. & Joos, F. Southern ocean anthropogenic carbon sink constrained by sea surface salinity. *Sci. Adv.* **7**, eabd5964 (2021).
64. Terhaar, J. et al. Assessment of Global Ocean Biogeochemistry Models for ocean carbon sink estimates in RECCAP2 and recommendations for future studies. *J. Adv. Model. Earth Syst.* **16**, e2023MS003840 (2024).
65. Gloege, L. et al. Quantifying errors in observationally based estimates of ocean carbon sink variability. *Glob. Biogeochem. Cycles* **35**, e2020GB006788 (2021).
66. Hauck, J. et al. Sparse observations induce large biases in estimates of the global ocean CO₂ sink: an ocean model subsampling experiment. *Philos. Trans. R. Soc. A: Math. Phys. Eng. Sci.* **381**, 20220063 (2023).
67. Swart, N. C., Fyfe, J. C., Gillett, N. & Marshall, G. J. Comparing trends in the southern annular mode and surface westerly jet. *J. Clim.* **28**, 8840–8859 (2015).
68. Lee, S. K. et al. Human-induced changes in the global meridional overturning circulation are emerging from the Southern Ocean. *Commun. Earth Environ.* **4**, 69 (2023).
69. Waugh, D. W., Primeau, F., DeVries, T. & Holzer, M. Recent changes in the ventilation of the southern oceans. *Science* **339**, 568–570 (2013).
70. Waugh, D. W., Hogg, A. M., Spence, P., England, M. H. & Haine, T. W. N. Response of Southern Ocean ventilation to changes in midlatitude westerly winds. *J. Clim.* **32**, 5345–5361 (2019).
71. Patara, L., Böning, C. W. & Tanhua, T. Multidecadal changes in Southern Ocean ventilation since the 1960s driven by wind and buoyancy forcing. *J. Clim.* **34**, 1485–1502 (2021).
72. Biastoch, A. et al. Regional imprints of changes in the atlantic meridional overturning circulation in the eddy-rich ocean model VIKING20X. *Ocean Sci.* **17**, 1177–1211 (2021).
73. Sarmiento, J. L., Gruber, N., Brzezinski, M. A. & Dunne, J. P. High-latitude controls of thermocline nutrients and low latitude biological productivity. *Nature* **427**, 56–60 (2004).
74. Talley, L. D. et al. Changes in ocean heat, carbon content, and ventilation: a review of the first decade of GO-SHIP global repeat hydrography. *Annu. Rev. Mar. Sci.* **8**, 185–215 (2016).
75. Lenton, A. et al. Stratospheric ozone depletion reduces ocean carbon uptake and enhances ocean acidification. *Geophys. Res. Lett.* **36**, L12606 (2009).
76. Schmidtko, S., Heywood, K. J., Thompson, A. F. & Aoki, S. Multidecadal warming of Antarctic waters. *Science* **346**, 1227–1231 (2014).
77. Roemmich, D. et al. Unabated planetary warming and its ocean structure since 2006. *Nat. Clim. Change* **5**, 240–245 (2015).
78. Dhomse, S. S. et al. Estimates of ozone return dates from chemistry-climate model initiative simulations. *Atmos. Chem. Phys.* **18**, 8409–8438 (2018).
79. Plattner, G. K. et al. Long-term climate commitments projected with climate-carbon cycle models. *J. Clim.* **21**, 2721–2751 (2008).
80. Frölicher, T. L. & Joos, F. Reversible and irreversible impacts of greenhouse gas emissions in multi-century projections with the NCAR global coupled carbon cycle-climate model. *Clim. Dyn.* **35**, 1439–1459 (2010).

81. Gillett, N. P., Arora, V. K., Zickfeld, K., Marshall, S. J. & Merryfield, W. J. Ongoing climate change following a complete cessation of carbon dioxide emissions. *Nat. Geosci.* **4**, 83–87 (2011).
82. Marzeion, B., Kaser, G., Maussion, F. & Champollion, N. Limited influence of climate change mitigation on short-term glacier mass loss. *Nat. Clim. Change* **8**, 305–308 (2018).
83. Douville, H. et al. Water cycle changes. In Masson-Delmotte, V. et al. (eds.) *Climate Change 2021: The Physical Science Basis. Contribution of Working Group I to the Sixth Assessment Report of the Intergovernmental Panel on Climate Change*, 1055–1210 (Cambridge University Press, Cambridge, United Kingdom and New York, NY, USA, 2021).
84. Davila, X. et al. On the origins of open ocean oxygen minimum zones. *J. Geophys. Res. Oceans* **128**, e2023JC019677 (2023).
85. Madec, G. & the NEMO team. NEMO ocean engine. In: *Note du Pôle de modélisation de l'Institut Pierre-Simon Laplace (IPSL)* No. 27 (2016).
86. Barnier, B. et al. Impact of partial steps and momentum advection schemes in a global ocean circulation model at eddy-permitting resolution. *Ocean Dyn.* **56**, 543–567 (2006).
87. Hallberg, R. Using a resolution function to regulate parameterizations of oceanic mesoscale eddy effects. *Ocean Model.* **72**, 92–103 (2013).
88. Kriest, I. & Oschlies, A. MOPS-1.0: towards a model for the regulation of the global oceanic nitrogen budget by marine biogeochemical processes. *Geosci. Model Dev.* **8**, 2929–2957 (2015).
89. Chien, C. et al. FOCI-MOPS v1 - integration of marine biogeochemistry within the flexible ocean and climate infrastructure version 1 (FOCI 1) earth system model. *Geosci. Model Dev.* **15**, 5987–6024 (2022).
90. Kriest, I. et al. One size fits all? Calibrating an ocean biogeochemistry model for different circulations. *Biogeosciences* **17**, 3057–3082 (2020).
91. Levitus, S. Introduction. Vol. 1, World Ocean Database 1998. *NOAA Atlas NESDIS 18* <https://repository.library.noaa.gov/view/noaa/49345> (1998).
92. Garcia, H. E. et al. World Ocean Atlas 2013, Volume 3: dissolved oxygen, apparent oxygen utilization, and oxygen saturation. *NOAA Atlas NESDIS 75* <https://repository.library.noaa.gov/view/noaa/14849> (2014).
93. Garcia, H. E. et al. World Ocean Atlas 2013, Volume 4: dissolved inorganic nutrients (phosphate, nitrate, silicate). *NOAA Atlas NESDIS 76* <https://repository.library.noaa.gov/view/noaa/14850> (2014).
94. Lavuset, S. K. et al. A new global interior ocean mapped climatology: the 1°x1° GLODAP version 2. *Earth Syst. Sci. Data* **8**, 325–340 (2016).
95. Buchanan, P. J. & Tagliabue, A. The regional importance of oxygen demand and supply for historical ocean oxygen trends. *Geophys. Res. Lett.* **48**, e2021GL094797 (2021).
96. Segschneider, J. & Bendtsen, J. Temperature-dependent remineralization in a warming ocean increases surface pCO₂ through changes in marine ecosystem composition. *Glob. Biogeochem. Cycles* **27**, 1214–1225 (2013).
97. Rabalais, N. N. Ocean deoxygenation from eutrophication (human nutrient inputs). In: Laffoley, D. & Baxter, J. M. (eds.) *Ocean deoxygenation: Everyone's problem - Causes, impacts, consequences and solutions*, 117–135 (Gland, Switzerland: IUCN, 2019).
98. Basterretxea, G., Font-Muñoz, J. S., Hernández-Carrasco, I. & Sañudo-Wilhelmy, S. Global variability of high-nutrient low-chlorophyll regions using neural networks and wavelet coherence analysis. *Ocean Sci.* **19**, 973–990 (2023).
99. Browning, T. J. et al. Persistent equatorial Pacific iron limitation under ENSO forcing. *Nature* **621**, 330–335 (2023).
100. Stewart, K. D. et al. JRA55-do-based repeat year forcing datasets for driving ocean-sea-ice models. *Ocean Model.* **147**, 101557 (2020).
101. Mayot, N. et al. Climate-driven variability of the Southern Ocean CO₂ sink. *Philos. Trans. R. Soc. A Math. Phys. Eng. Sci.* **381**, 20220055 (2023).
102. Garcia, H. E. & Gordon, L. I. Oxygen solubility in seawater: better fitting equations. *Limnol. Oceanogr.* **37**, 1307–1312 (1992).
103. Good, S. A., Martin, M. J. & Rayner, N. A. EN4: quality controlled ocean temperature and salinity profiles and monthly objective analyses with uncertainty estimates. *J. Geophys. Res. Oceans* **118**, 6704–6716 (2013).
104. Cheng, L. et al. Improved estimates of ocean heat content from 1960 to 2015. *Sci. Adv.* **3**, e1601545 (2017).
105. Levitus, S. et al. World ocean heat content and thermosteric sea level change (0–2000 m), 1955–2010. *Geophys. Res. Lett.* **39**, L10603 (2012).
106. Müller, J. D. RECCAP2-ocean data collection [dataset] <https://doi.org/10.5281/zenodo.7990823> (2023).
107. Ziehn, T. et al. The Australian earth system model: ACCESS-ESM1.5. *J. South. Hemisph. Earth Syst. Sci.* **70**, 193–214 (2020).
108. Christian, J. R. et al. Ocean biogeochemistry in the canadian earth system model version 5.0. 3: Canesm5 and canesm5-canoe. *Geosci. Model. Dev. Discuss.* **2021**, 1–68 (2021).
109. Séférian, R. et al. Evaluation of CNRM earth system model, CNRM-ESM2-1: role of earth system processes in present-day and future climate. *J. Adv. Model. Earth Syst.* **11**, 4182–4227 (2019).
110. Held, I. M. et al. Structure and performance of GFDL's CM4.0 climate model. *J. Adv. Model. Earth Syst.* **11**, 3691–3727 (2019).
111. Dunne, J. P. et al. The GFDL Earth System Model version 4.1 (GFDL-ESM 4.1): overall coupled model description and simulation characteristics. *J. Adv. Model. Earth Syst.* **12**, e2019MS002015 (2020).
112. Stock, C. A. et al. Ocean biogeochemistry in GFDL's Earth System Model 4.1 and its response to increasing atmospheric CO₂. *J. Adv. Model. Earth Syst.* **12**, e2019MS002043 (2020).
113. Giorgetta, M. A. et al. Climate and carbon cycle changes from 1850 to 2100 in MPI-ESM simulations for the coupled model intercomparison project phase 5. *J. Adv. Model. Earth Syst.* **5**, 572–597 (2013).
114. Mauritsen, T. et al. Developments in the MPI-M earth system model version 1.2 (MPI-ESM1.2) and its response to increasing CO₂. *J. Adv. Model. Earth Syst.* **11**, 998–1038 (2019).
115. Riahi, K. et al. The shared socioeconomic pathways and their energy, land use, and greenhouse gas emissions implications: an overview. *Glob. Environ. Change* **42**, 153–168 (2017).
116. Patara, L. & Hollitzer, H. A. L. Model output used in Hollitzer et al. (2024): competing effects of wind and buoyancy forcing on ocean oxygen trends in recent decades [dataset] (2024).

Acknowledgements

The ocean model simulations were integrated at the North German Supercomputing Alliance (HLRN). H.A.L.H. and J.T. acknowledge funding from the Swiss National Science Foundation under grant #PZ00P2_209044 (ArcticECO). L.P. acknowledges funding from the German Research Foundation under grant PA 3075/2-1. A.O. acknowledges stimulating discussions with members of the Global Ocean Oxygen Network (GO₂NE) expert working group of the Intergovernmental Oceanographic Commission of UNESCO (IOC-UNESCO). The authors thank Linus Vogt for providing the O₂ and OHC time series from the ESMs. EN4 temperature and salinity data were obtained from <https://www.metoffice.gov.uk/hadobs/en4/> and are ©British Crown Copyright, Met Office, 2024, provided under a Non-Commercial Government Licence <http://www.nationalarchives.gov.uk/doc/non-commercial-government-licence/version/2/>.

Author contributions

H.A.L.H. conceived and led the study, produced the figures, and wrote the initial manuscript under the supervision of L.P., A.O., and J.T. L.P. performed the experiments with ORCA025-MOPS. All authors contributed to the analysis and interpretation of the results and to the editing of the manuscript into its final draft.

Funding

Open Access funding enabled and organized by Projekt DEAL.

Competing interests

The authors declare no competing interests.

Additional information

Supplementary information The online version contains supplementary material available at

<https://doi.org/10.1038/s41467-024-53557-y>.

Correspondence and requests for materials should be addressed to Helene A. L. Hollitzer.

Peer review information *Nature Communications* thanks the anonymous reviewers for their contribution to the peer review of this work. A peer review file is available.

Reprints and permissions information is available at

<http://www.nature.com/reprints>

Publisher's note Springer Nature remains neutral with regard to jurisdictional claims in published maps and institutional affiliations.

Open Access This article is licensed under a Creative Commons Attribution 4.0 International License, which permits use, sharing, adaptation, distribution and reproduction in any medium or format, as long as you give appropriate credit to the original author(s) and the source, provide a link to the Creative Commons licence, and indicate if changes were made. The images or other third party material in this article are included in the article's Creative Commons licence, unless indicated otherwise in a credit line to the material. If material is not included in the article's Creative Commons licence and your intended use is not permitted by statutory regulation or exceeds the permitted use, you will need to obtain permission directly from the copyright holder. To view a copy of this licence, visit <http://creativecommons.org/licenses/by/4.0/>.

© The Author(s) 2024